The Astrophysical Journal Letters, 917:L20 (6pp), 2021 August 20 https://doi.org/10.3847/2041-8213/ac14bd

Magnetic Field Draping of the Heliopause and Its Consequences for Radio Emission in the Very Local Interstellar Medium

N. V. Pogorelov[1,2], F. Fraternale[2], T. K. Kim[2], L. F. Burlaga[3], and D. A. Gurnett[4]
[1] Department of Space Sciences, The University of Alabama in Huntsville, Huntsville, AL 35805, USA; nikolai.pogorelov@uah.edu
[2] Center for Space Plasma and Aeronomic Research, The University of Alabama in Huntsville, Huntsville, AL 35805, USA
[3] Leonard F. Burlaga, Inc., Davidsonville, MD 21035, USA
[4] Department of Physics and Astronomy, The University of Iowa, Iowa City, IA 52242, USA
Received 2021 May 20; revised 2021 June 30; accepted 2021 July 15; published 2021 August 17

Abstract

We discuss the observations and simulations related to the interaction of the solar wind (SW) and local interstellar medium (LISM), and the interstellar magnetic field draping around the heliopause (HP). This Letter sheds light on some processes that are not directly seen in the Voyager data. Special attention is paid to the magnetic field behavior at the HP crossing, penetration of shocks, and compression waves across the HP, and their merging in the LISM surrounding it. Modeling identifies forward and reverse shocks propagating through the heliosheath. Voyager data shows that the magnetic field strength experiences a jump at the HP, while the elevation and azimuthal angles are continuous across it. We show that our prior numerical results are in agreement with the Voyager data, if the heliospheric magnetic field is not assumed unipolar. The simulations confirm the importance of taking into account time dependencies of the SW flow, including the presence of transient structures and magnetohydrodynamic instabilities. For the first time, we provide the heliospheric community with the Alfvén speed distribution observed by Voyagers, which shows that it is unexpectedly small and decreases with distance from the HP. This is of critical importance for the identification of physical mechanisms responsible for the Langmuir wave and radio emission generation behind the HP. The data shows that outward-propagating, subcritical shocks traversing the LISM have a rather wide dissipation structure, which raises questions about their ability to reflect electrons as collisionless shocks can do.

Unified Astronomy Thesaurus concepts: Heliosphere (711); Interstellar medium (847); Heliosheath (710); Heliopause (707); Interstellar magnetic fields (845)

Supporting material: animations

1. Introduction

The structure and dynamical evolution of the heliosphere is governed by a number of fundamental physical processes that define how plasma and magnetic fields of solar origin interact with the local interstellar medium (LISM). The solar plasma is accelerated near the Sun and creates the solar wind (SW), which is collisionless with respect to Coulomb collisions. The part of the LISM affected by the presence of the heliosphere is called the very local interstellar medium (VLISM). The SW–LISM interaction creates a heliospheric termination shock (TS) and the heliopause (HP), both observed in situ by Voyager 1 (V1) and Voyager 2 (V2) spacecraft (Stone et al. 2005, 2008, 2013). The LISM plasma is collisional on scales of about 2–4 au (Fraternale & Pogorelov 2021). The LISM is partially ionized, so charge exchange between ions and atoms plays an important role in the SW–LISM interaction.

As new populations of neutral atoms are born in the SW and LISM, some of them can propagate far upstream into the LISM and modify it (Gruntman 1982). In addition, nonthermal (pickup) ions (PUIs) are created (Moebius et al. 1993; Gloeckler et al. 2009). They energetically dominate the SW at large heliocentric distances and in the inner heliosheath (IHS; the SW region between the TS and HP), create turbulence, and affect the properties of the TS and HP (Burlaga et al. 1994; Chalov et al. 1995; Richardson et al. 1995; Zank et al. 1996; Decker et al. 2008, 2015).

Numerical modeling is useful for reproducing, interpreting, and predicting observational data. Our knowledge of the SW properties at 1 au is incomplete to such extent that space weather is better predicted by data assimilation methods than by strict solutions to magnetohydrodynamic (MHD) equations (Jian et al. 2015). This creates challenges for the development of inner boundary conditions for the SW–LISM interaction analysis. The boundary conditions in the unperturbed LISM are mostly derived from the He atom observations (McComas et al. 2015). The current consensus is that the LISM temperature and velocity are ∼7000 K and 25.4 km s^{-1}, while the direction of its velocity has ecliptic longitude and latitude equal to 255.°7 and 5.°1, respectively. The direction and magnitude of the interstellar magnetic field (ISMF) vector, plasma, and neutral atom densities in the unperturbed LISM are not directly measured, but simulations provide us with guidelines for their choices (Zirnstein et al. 2016). The observed properties of the SW and VLISM plasma are time-dependent on different scales, including the difference between solar cycles, topological variations of the SW within each cycle, transient phenomena, turbulence, etc.

The ISMF direction immediately after V1 crossed the HP was predicted in Pogorelov et al. (2009a, their Figure 8) and Borovikov & Pogorelov (2014, their Figure 4). Here we show that our previous simulation results (Pogorelov et al. 2015, 2017b; Kim et al. 2017) also agree with the ISMF measurements at V1 and V2 across the HP. Using our analysis of simulations and spacecraft measurements, we discuss the mechanisms of plasma wave generation and radio emission in the VLISM.

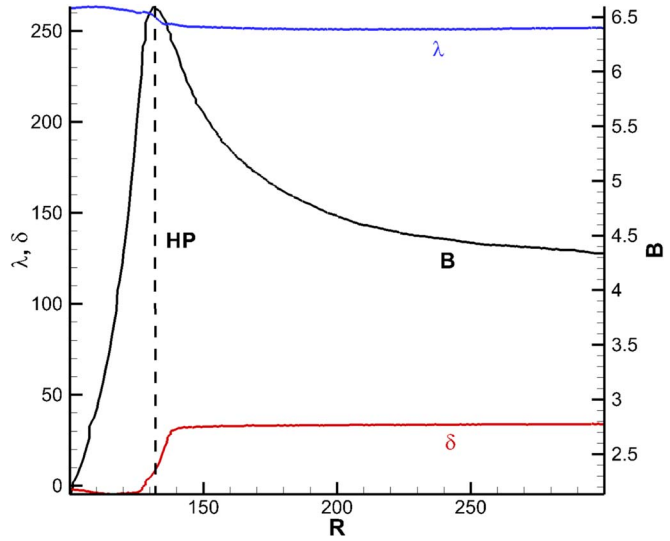

Figure 1. Distributions of magnetic field strength, $B = |\boldsymbol{B}|$, and the elevation and azimuthal angles, δ and λ, along the V2 trajectory in the SW–LISM interaction assuming unipolar heliospheric magnetic field (HMF).

2. ISMF Draping the Heliopause

The ISMF of the unperturbed LISM is substantially modified by the heliosphere. In the Sun's reference frame, the LISM flow behaves similarly to airflow over a blunt body. There are differences, however. First, the LISM flow is magnetized, so the characteristic wave system differs from that in gas dynamics. Second, the LISM is affected by secondary neutral atoms born in front of the TS (neutral SW, NSW) and in the IHS, and propagating outward. As a result, charge exchange decelerates the LISM and its temperature increases. Interestingly, a heliospheric boundary layer (HBL) is formed on the LISM side of the HP (Baranov & Malama 1993), which is seen as a layer of lower plasma density on the LISM side of the HP. The plasma distribution in the HBL is affected by the kinetic charge exchange between the LISM protons and H atoms. While the increase in density with distance from the HP has been attributed to the presence of a depletion layer (Fuselier & Cairns 2013), it should not be expected to have maximum at the HP surface anywhere, except for the stagnation point, even without magnetic field and charge exchange. This is because it is the entropy that has the maximum value on the surface of a blunt body, such as the HP, inserted into a gas flow, not the density. Voyagers now remain in the HBL, as the plasma wave frequency observed by the Plasma Wave System (PWS) continues to increase on the average, while the exact monotonicity is not exactly preserved due to time-dependent phenomena (Gurnett et al. 2015).

A puzzling element of the V1 and V2 observations is the absence of rotation of the magnetic field vector across the HP. We analyze the ISMF draping in our previous simulations in an attempt to understand this phenomenon. Pogorelov et al. (2017b) simulated the distributions of the ISMF vector magnitude, B, and its elevation and azimuthal angles, δ and λ, in the direction of V1 trajectory. Those steady-state, MHD plasma/kinetic neutrals simulations were performed for different properties of the unperturbed LISM, including the ISMF direction and magnitude agreeable with the IBEX observations (Zirnstein et al. 2016). Figure 1 shows a similar distribution in the direction of the V2 trajectory, but only for $B_\infty = 3\ \mu$G in the unperturbed LISM. It is assumed that the heliospheric magnetic field (HMF) is unipolar. This approach was proposed by Czechowski et al. (2010) to avoid issues with the resolution of the thin heliospheric current sheet (HCS), especially in the region between the TS and HP, where the sector width substantially decreases. The intention was to insert the HCS into the unipolar solution a posteriori assuming that its surface passively propagates with the SW plasma. In practice, the latter approach turned out to be challenging, because the classical HCS dissipates in some regions of the heliosphere (Richardson et al. 2016). As a consequence, simulation results with the partially unresolved HCS and corresponding lower magnetic field strengths agree with observations better than those using the unipolar HMF (Pogorelov et al. 2013). As seen from Figure 1, such approach makes the distributions of B, λ, and δ incompatible with observations. In particular, B is monotonically increasing after V2 crosses the TS and reaches maximum at the HP. A similar feature is seen in Izmodenov & Alexashov (2020). There is no clear jump in B across the HP (numerically smeared over 5 au), while the elevation and azimuthal angles are different on its SW and LISM sides. In addition, the plasma β is unrealistically small (0.2–0.25) in the SW near the HP. Note that the assumption of unipolar HMF is essential for the numerical scenario that involves splitting of the heliotail into two branches (Opher et al. 2015; Pogorelov et al. 2015, 2017a).

Steady-state solutions are not ideal for comparison with observational data. Both the solar cycle variations and differences between different solar cycles have imprints in the observational data. Moreover, according to Florinski (2015), the HP instabilities may decrease the difference in the magnetic field vector directions on the SW and LISM sides of the HP. This motivates us to use our prior multi-fluid solutions of the SW–LISM interaction problem that were able to resolve (numerical grid $\sim$0.4 au^3) such instability in three dimensions (Pogorelov et al. 2017b). These simulations are not entirely data driven, because we use a nominal solar cycle approach where the SW is split into the slow and fast wind regions, the boundary between them being a function of time, so that the latitudinal extent of the slow wind is smallest during solar activity minima and largest at activity maxima. In addition, the tilt of the Sun's magnetic axis with respect to its rotation axis also increases monotonically from a small value to 90° flipping to the opposite polarity exactly at the solar activity maxima (Pogorelov et al. 2009a).

Figure 2 shows the distributions of B, λ, and δ in the planes formed by the Sun's rotation axis (z-axis) and the V1 (left panels) and V2 trajectories, respectively. In agreement with the observational data, there is a jump in the magnetic field strength, while the ISMF elevation and azimuthal angle are continuous across the HP. This is even better seen in Figure 3, where the distribution of the same quantities is shown along the V1 (top panel) and V2 (bottom panel) trajectories. While this is just one of the time-evolution frames, the animated Figure 3 shows that such behavior is not unusual, and similar distributions are observed frequently. It is seen from the animations that rotations of the magnetic field vector across the HP cannot be excluded, particularly due to periodic changes of the HMF polarity. In accord with the spacecraft observations, the elevation and azimuthal angles rather smoothly evolve with distance from the HP. The obtained angles are slightly different from those observed, which is not surprising due to uncertainties in the boundary conditions. These uncertainties have been discussed recently by Swaczyna et al. (2021) in the

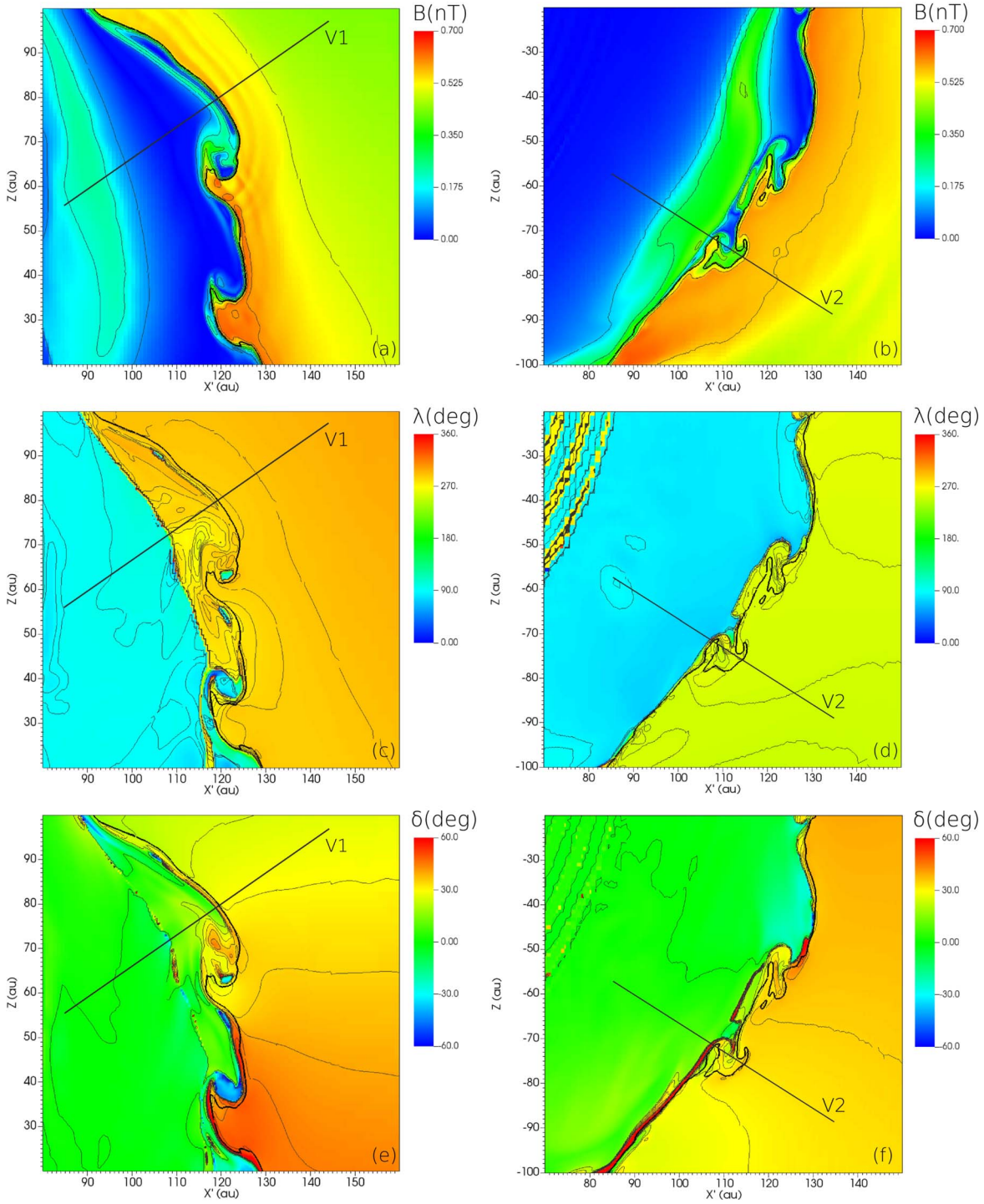

Figure 2. Distributions of the magnetic field strength, and the elevation and azimuthal angles (δ and λ) in the planes formed by the z-axis and the V1 (left panels) and V2 (right panels) trajectories.

context of possible collisional heating and deceleration of He atoms arriving into the heliosphere from the pristine LISM.

Kim et al. (2017) performed a data-driven (based on OMNI data and variable coronal hole size boundary conditions) simulation of the SW–LISM interaction and showed that some of the shocks observed by V1 can be well reproduced. It was also shown that each shock created at the HP and propagating upstream into the LISM decreases in intensity and speed as it propagates radially outward, and ultimately disappears at some distance from the HP. This is not surprising for radially propagating disturbances. A shock can become stronger only when one shock overtakes another. Such shock interaction is given in Figure 4(b) (and its animation) of the magnetic field distribution along the V1 trajectory. Here we show both the time frames and the quantities taken by a virtual probe (indicated at each moment of time with a blue circle) co-moving with the V1 along its trajectory. The observations are shown with the green line.

Figure 4(a) shows the distribution of $|\boldsymbol{B}|$, δ, and λ as a function of time along the V1 trajectory. The observational data

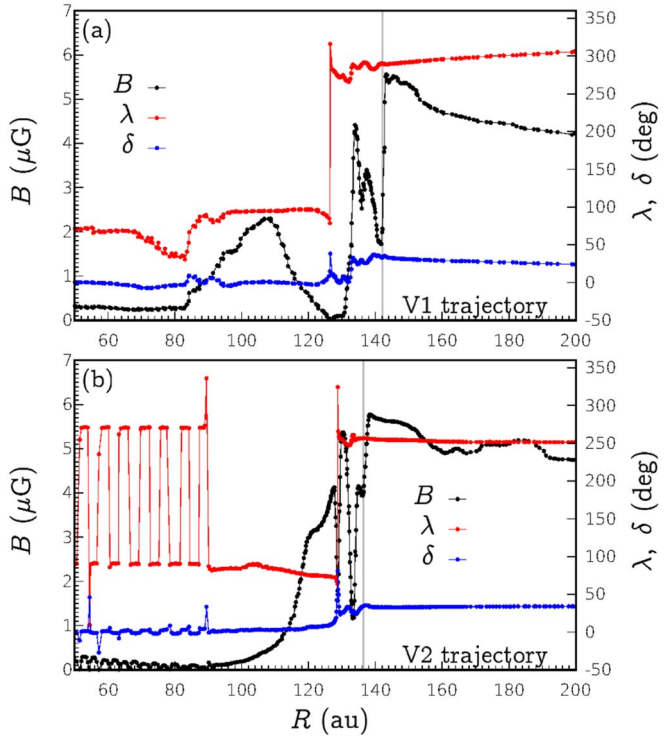

Figure 3. Snapshot of the distribution of magnetic field strength, B, and the elevation and azimuthal angles, δ and λ, along the V1 (panel (a)) and V1 (panel (b)) trajectories in the SW–LISM simulation featuring the HP instability. The animated figure shows these over the interval of 50 yr. The realtime duration of the animation is 22 s.

(An animation of this figure is available.)

and simulation results are shown with solid and dashed lines, respectively. Although the simulated distributions are not in full agreement with the observations, one can see that δ and λ are continuous across the HP, which is shown with the vertical lines. Their values asymptotically approach those observed by the spacecraft. However, the angles do change considerably in the SW region adjacent to the HP.

It is of interest that both V1 and V2 typically observe clear, almost linear decreases in B immediately after being overtaken by shocks, or compression waves (Burlaga & Ness 2016; Burlaga et al. 2020). This happens because these shocks propagate outward into the region of globally decreasing B. As seen from the top panel of the animated Figure 4(b), the likelihood of the spacecraft to observe shock overtaking is small, but not negligible. Besides, it cannot be excluded that each individual, smaller-amplitude shock participating in the interaction cannot be resolved in the data. In particular, our simulations show that V1 could observe such merged shocks, or steepening pressure waves, at the beginning of 2020. Figure 4(b) shows that the structure of the merged shock is initially wider than those for each individual shock. It is of interest that a region of rather small perturbations is following the latest merged shock and is expected to overtake V1—a feature similar to that described in Burlaga et al. (2021).

The bottom panel of Figure 4 and its animation show the distributions of the thermal and magnetic pressures, $p_{\rm th}$ and $p_{\rm mag}$, their sum, and ram pressure. The dashed and solid lines correspond to different time moments to demonstrate the shocks propagating downstream (panel (c)) and upstream (panel (d)) in the IHS. This animation shows how IHS perturbations and shocks cross the HP, exhibiting decreases in $p_{\rm th}$ and increases in $p_{\rm mag}$, while preserving the total pressure, in agreement with data.

3. Plasma Waves and Radio Emission in the HBL

There is a close association between the electron plasma oscillations (Gurnett et al. 2013) and the jumps in the magnetic field strength (Burlaga et al. 2013) observed in the HBL. According to PWS measurements (Gurnett et al. 2015), V1 observed radio emission in the 2–3 kHz range, which is thought to be excited by shocks propagating through plasma regions primed with nonthermal electrons resonantly accelerated by lower hybrid (LH) waves driven by a ring-beam instability of PUIs (Gurnett et al. 1993; Cairns & Zank 2002; Fuselier & Cairns 2013). Further acceleration of these electrons by a propagating shock may create electron beams moving away from it. These beams produce Langmuir waves, via the "bump-on-tail" instability—a concept first proposed by Filbert & Kellogg (1979) and later refined by Cairns (1987). For a shock front convex outward with respect to the incoming plasma flow, the bump-on-tail velocity distribution is due to the existence of a threshold velocity below which electrons cannot reach a given point upstream of the shock. The region accessible to such beams is called the electron foreshock. Mitchell et al. (2009) and Pogorelov et al. (2009b) suggested that PUIs that created nonthermal electrons may originate not from the hot IHS atoms (Cairns & Zank 2002), but from the NSW. However, the presence of nonthermal electrons is insufficient for the development LH instability. The propagation of a shock through the LISM can cause radio emission only if the instability growth rate and energy transfer to electrons are sufficient, which occurs (see Cairns & Zank 2002, and references therein) if $\alpha_{\rm r} = V_{\rm r}/V_{\rm A} < 5$, where $V_{\rm r}$ and $V_{\rm A}$ are the PUI ring-beam and Alfvén speeds, respectively. Magnetic field draping around the HP creates conditions for larger $V_{\rm A}$. For PUIs born in the HBL by charge exchange of the LISM ions with the NSW, which actually have a ring-beam distribution, $V_{\rm r}$ should be ~400 km s. If this process involves hot, secondary H atoms born in the IHS, $V_{\rm r} \approx 100\,{\rm km\,s^{-1}}$.

Pogorelov et al. (2008, 2009b) considered two possible scenarios: (1) the LH instability criterion is not satisfied in the HBL unless there is a shock propagating through it and producing magnetic field enhancements; (2) for stronger B_∞, the criterion can be always satisfied, so that any shock propagating through the HBL will generate plasma oscillations and, possibly, radio emission events. V1 data provide us with a new perspective on the plasma wave and radio emission generation. Figure 5 shows the distribution of the Alfvén speed along the V1 (blue line) and V2 (red line) trajectories. The time at V2 is shifted by 6.2 yr backward in time, and $V_{\rm A}$ at V2 is scaled by the factor of 0.5. It is seen that $V_{\rm A}$ decreases with distance from the HP, and is below $45\,{\rm km\,s^{-1}}$ at V1 and $85\,{\rm km\,s^{-1}}$ at V2 immediately after the HP. The Alfvén speed increases across the shocks traversing the HBL, but not substantially, because all shocks observed in the HBL so far were rather weak. Therefore, it is unlikely that $\alpha_{\rm r}$ would be smaller than 5 for ring-beam velocities corresponding to the NSW. Although this means that the scenario associated with PUIs born from the hot IHS neutral atoms, which have lower $V_{\rm r}$, returns, there remains a question about the physical mechanisms responsible for the plasma wave and radio emission generation, as Roytershteyn et al. (2019) reported

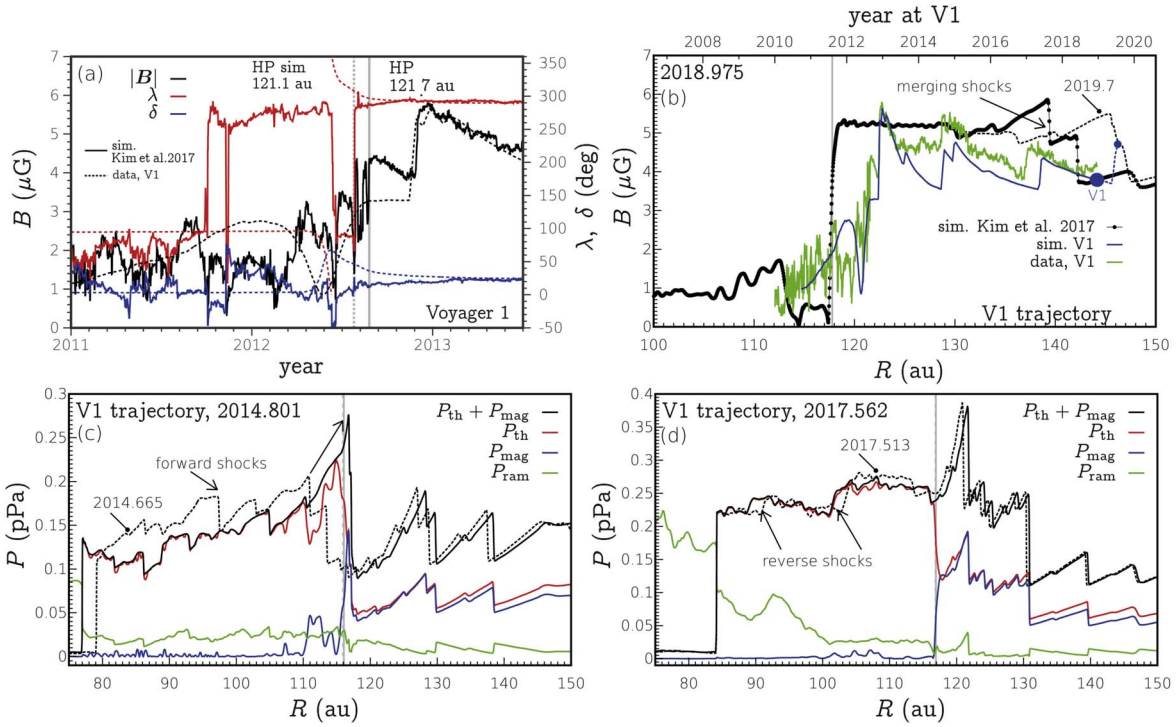

Figure 4. Panel (a): snapshot of the magnetic field strength, and its elevation and azimuthal angles in the vicinity of the HP crossing measured by V1 (solid lines) and simulated in Kim et al. (2017; dashed lines). The vertical lines show the HP position at the moment of V1 entering the LISM. Panel (b): two shocks approaching each other before merging in the HBL. The blue and green lines show the magnetic field distribution at a virtual V1 moving through the solution and the data, respectively. Panels (c) and (d): two time frames with the pressure distributions along the V1 trajectory show the forward and reverse shocks propagating through the IHS. The dashed lines correspond to slightly shifted moments of time. The animated figure shows panels (b) and (c) over the time interval 2010–2021 with a 15 day cadence. The realtime duration of the animation is 23 s.

(An animation of this figure is available.)

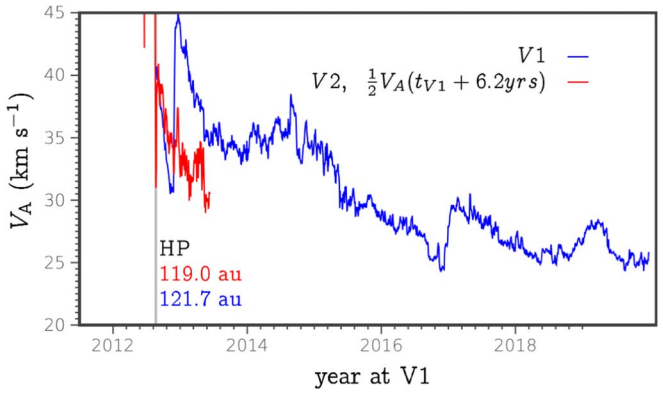

Figure 5. Distribution of the Alfvénic speed along the V1 (blue line) and V2 (red line) trajectories calculated using the MAG and PWS measurements. V2 data are scaled by the factor of 0.5 and shifted by 6.2 yr.

no substantial LH instability for a realistic, three-component distribution of PUIs in the HBL.

The Voyager magnetometers cannot resolve high-frequency magnetic field turbulence related to electron foreshocks. Fraternale et al. (2020) identified an enhanced turbulence level in front of the shock observed by V1 at 2014.65, which can potentially be attributed to ion reflection. However, all other shocks crossing V1 did not show such turbulence enhancements. Moreover, not all observed plasma wave events can be associated with the shocks (or compression waves) observed by MAG (Burlaga et al. 2021). The difference in their widths is possibly indicative of the absence of steady dissipative structure in all shocks propagating through the evolving LISM background. The shock described in Fraternale et al. (2020) is quasi-perpendicular, has rather low compression ratio, and is subcritical (Burlaga & Ness 2016). Fraternale & Pogorelov (2021) estimated the shock width to be ∼0.044 au, which corresponds to about 10^4 proton inertial lengths. The question remains whether shocks that wide can reflect electrons as collisionless shocks can do.

4. Conclusions

We have shown that time-dependent simulations do not contradict observational data in situations when there is no region of single-polarity HMF in the immediate vicinity of the HP on its heliospheric side. The situation is different in the opposite case, which is especially well seen when the heliospheric magnetic field is assumed to be unipolar, as in the solutions resulting in the heliotail splitting. In this case, $|\boldsymbol{B}|$ becomes continuous across the HP, while the angles do not. Such continuity of the magnetic field strength necessarily requires low plasma beta on its both sides, which was not observed.

As far as the continuity of the magnetic field direction across the HP is concerned, a few observations can be made: (1) the smeared jumps of δ and λ may be related to large-scale instabilities or, in general, nonstationary HP; (2) the smearing can be enhanced by turbulence in situations when the amplitude of fluctuations of δ and λ on the inner side of the HP is comparable to the average values; (3) the HP motion radially outwards can make jumps appear more smeared in observations.

By combining the MAG and PWS data, we were able to calculate the distribution of the Alfvén speed along the V1 and V2 trajectories. It was determined that this velocity is too small to satisfy the previously derived criterion for an efficient energy transfer to electrons through the LH drive. This conclusion is especially applicable to the scenario in which plasma waves and radio emission in the HBL are initiated by PUIs born from the NSW. Additional efforts should be undertaken to shed light onto the electron acceleration mechanism in the vicinity of "thick" subcritical shocks overtaking the Voyager spacecraft in the HBL.

This work is supported by NASA grants 80NSSC19K0260, 80NSSC18K1649, 80NSSC18K1212, and NSF-BSF grant PHY-2010450. N.P. was also partially supported by the IBEX mission as a part of NASA's Explorer program. L.F.B. was supported by NASA contract 80GSFC19C0012. The research at the University of Iowa was supported by NASA through contract 1622510 with the Jet Propulsion Laboratory. The authors acknowledge the Texas Advanced Computing Center (TACC) at The University of Texas at Austin for providing HPC resources on Frontera supported by NSF LRAC award 2031611. Supercomputer time allocations were also provided on SGI Pleiades by NASA High-End Computing Program award SMD-17-1537 and Stampede2 by NSF XSEDE project MCA07S033. We acknowledge the NASA Space Physics Data Facility (https://cohoweb.gsfc.nasa.gov/coho/).

ORCID iDs

N. V. Pogorelov https://orcid.org/0000-0002-6409-2392
F. Fraternale https://orcid.org/0000-0002-4700-2762
T. K. Kim https://orcid.org/0000-0003-0764-9569
L. F. Burlaga https://orcid.org/0000-0002-5569-1553
D. A. Gurnett https://orcid.org/0000-0003-2403-0282

References

Baranov, V. B., & Malama, Y. G. 1993, JGR, 98, 15157
Borovikov, S. N., & Pogorelov, N. V. 2014, ApJL, 783, L16
Burlaga, L. F., Kurth, W. S., Gurnett, D. A., et al. 2021, ApJ, 911, 61
Burlaga, L. F., & Ness, N. F. 2016, ApJ, 829, 134
Burlaga, L. F., Ness, N. F., Belcher, J. W., et al. 1994, JGR, 99, 21511
Burlaga, L. F., Ness, N. F., Berdichevsky, D. B., et al. 2020, AJ, 160, 40
Burlaga, L. F., Ness, N. F., & Stone, E. C. 2013, Sci, 341, 147
Cairns, I. H. 1987, JGR, 92, 2315
Cairns, I. H., & Zank, G. P. 2002, GeoRL, 29, 1143
Chalov, S. V., Fahr, H. J., & Izmodenov, V. 1995, A&A, 304, 609
Czechowski, A., Strumik, M., & Grygorczuk, J. 2010, A&A, 516, 17
Decker, R. B., Krimigis, S. M., Roelof, E. C., et al. 2008, Natur, 454, 67
Decker, R. B., Krimigis, S. M., Roelof, E. C., & Hill, M. E. 2015, JPhCS, 577, 012006
Filbert, P. C., & Kellogg, P. J. 1979, JGR, 84, 1369
Florinski, V. 2015, ApJ, 813, 49
Fraternale, F., & Pogorelov, N. V. 2021, ApJ, 906, 75
Fraternale, F., Pogorelov, N. V., & Burlaga, L. F. 2020, ApJL, 897, L28
Fuselier, S. A., & Cairns, I. H. 2013, ApJ, 771, 83
Gloeckler, G., Fisk, L. A., Geiss, J., et al. 2009, SSRv, 143, 163
Gruntman, M. A. 1982, SvAL, 8, 24
Gurnett, D. A., Kurth, W. S., Allendorf, S. C., & Poynter, R. L. 1993, Sci, 262, 199
Gurnett, D. A., Kurth, W. S., Burlaga, L. F., & Ness, N. F. 2013, Sci, 341, 1489
Gurnett, D. A., Kurth, W. S., Stone, E. C., et al. 2015, ApJ, 809, 121
Izmodenov, V. V., & Alexashov, D. B. 2020, A&A, 633, L12
Jian, L. K., MacNeice, P. J., Taktakishvili, A., et al. 2015, SpWea, 13, 316
Kim, T. K., Pogorelov, N. V., & Burlaga, L. F. 2017, ApJL, 843, L32
McComas, D. J., Bzowski, M., Frisch, P., et al. 2015, ApJ, 801, 28
Mitchell, J. J., Cairns, I. H., & Heerikhuisen, J. 2009, GeoRL, 36, L12109
Moebius, E. D., Hovestadt, B., Klecker, D., Scholer, M., & Gloeckler, G. 1993, Natur, 318, 426
Opher, M., Drake, J. F., Zieger, B., & Gombosi, T. I. 2015, ApJL, 800, 28
Pogorelov, N. V., Borovikov, S. N., Heerikhuisen, J., & Zhang, M. 2015, ApJL, 812, L6
Pogorelov, N. V., Borovikov, S. N., Zank, G. P., & Ogino, T. 2009a, ApJ, 696, 1478
Pogorelov, N. V., Fichtner, H., Czechowski, A., et al. 2017a, SSRv, 212, 193
Pogorelov, N. V., Heerikhuisen, J., Mitchell, J. J., Cairns, I. H., & Zank, G. P. 2009b, ApJL, 695, L31
Pogorelov, N. V., Heerikhuisen, J., Roytershteyn, V., et al. 2017b, ApJ, 845, 9
Pogorelov, N. V., Heerikhuisen, J., & Zank, G. P. 2008, ApJL, 675, L41
Pogorelov, N. V., Suess, S. T., Borovikov, S. N., et al. 2013, ApJ, 772, 2
Richardson, J. D., Burlaga, L. F., Drake, J. F., Hill, M. E., & Opher, M. 2016, ApJ, 831, 115
Richardson, J. D., Paularena, K. I., Lazarus, A. J., & Belcher, J. W. 1995, GeoRL, 22, 1469
Roytershteyn, V., Pogorelov, N. V., & Heerikhuisen, J. 2019, ApJ, 881, 65
Stone, E. C., Cumminghs, A. C., McDonald, F. B., et al. 2008, Natur, 454, 71
Stone, E. C., Cummings, A. C., McDonald, F. B., et al. 2005, Sci, 309, 2017
Stone, E. C., Cummings, A. C., McDonald, F. B., et al. 2013, Sci, 341, 150
Swaczyna, P., Rahmanifard, F., Zirnstein, E. J., McComas, D. J., & Heerikhuisen, J. 2021, ApJL, 911, L36
Zank, G. P., Pauls, H. L., Cairns, I. H., & Webb, G. M. 1996, JGR, 101, 457
Zirnstein, E. J., Heerikhuisen, J., Funsten, H. O., et al. 2016, ApJL, 818, L18